

## Symmetry-breaking perturbations and strange attractors

Anna Litvak-Hinenzon\* and Vered Rom-Kedar†

The Faculty of Mathematical Sciences, The Weizmann Institute of Science, P.O. Box 26, Rehovot 76100, Israel

(Received 28 October 1996)

The asymmetrically forced, damped Duffing oscillator is introduced as a prototype model for analyzing the homoclinic tangle of symmetric dissipative systems with *symmetry-breaking* disturbances. Even a slight fixed asymmetry in the perturbation may cause a substantial change in the asymptotic behavior of the system, e.g., transitions from two-sided to one-sided strange attractors as the other parameters are varied. Moreover, slight asymmetries may cause substantial differences in the relative size of the basins of attraction of the two wells. These changes seem to be associated with homoclinic bifurcations. Numerical evidence indicates that *strange attractors* appear near curves corresponding to specific secondary homoclinic bifurcations. These curves are found using analytical perturbational tools. [S1063-651X(97)00804-0]

PACS number(s): 05.45+b, 02.30.Hq, 46.90.+s

### I. INTRODUCTION

The forced and damped Duffing oscillator

$$\ddot{x} + \varepsilon \delta \dot{x} - x + x^3 = \varepsilon \gamma \cos(\omega t), \quad (x, t) \in \mathfrak{R}^1 \times \mathfrak{R}^1, \quad (1)$$

has served as a prototype model for investigating low dimensional chaotic behavior in numerous publications (see [1–4], and references therein). Its significance lies in its simple “typical form” which appears in many applications. Indeed, the unperturbed Duffing oscillator represents the normal form for Hamiltonian systems with  $Z_2$  symmetry [5]. Thus whether different types of perturbations lead to substantially different dynamics is of mathematical and physical significance. The perturbation of Eq. (1) has two specific properties—it has no nonlinear terms in  $x, \dot{x}$  and it is symmetric; Eq. (1) is invariant under  $x \rightarrow -x, t \rightarrow t + \pi/\omega$ .

Numerical simulations suggest that the inclusion of a nonlinear dissipation term in the perturbation does not alter the qualitative behavior of the forced system [6]. Namely, no new bifurcation sequences or new types of attractors appear, though the location of the various bifurcation curves of Eq. (1) changes. The effect of asymmetric potentials has been investigated when the forcing is adiabatic, see [7,8], and references therein. In this paper we examine the effect of asymmetric forcing on the Duffing oscillator by introducing the *asymmetrically forced, damped, Duffing oscillator* (AFDO):

$$\begin{aligned} \ddot{x} + \delta \dot{x} - x + x^3 &= (x - \beta x^2) \gamma \cos(\omega t), \\ (x, t) &\in \mathfrak{R}^1 \times \mathfrak{R}^1, \end{aligned} \quad (2)$$

which contains the asymmetry perturbation parameter  $\beta$ . Here we show that the inclusion of the *physically typical* asymmetric forcing perturbations alters the *qualitative* behavior of the system in some range of parameter values.

Theoretical and numerical investigation of forced and damped systems with homoclinic tangle is problematic since

these may attain strange attractors (SAs) and periodic sinks simultaneously. [SAs are attractors with sensitive dependence on initial conditions, i.e., attractors which have a dense orbit with positive Lyapunov exponent (see [9]).] Moreover, the existence of the SA is extremely sensitive to changes in parameter values. The existence of Newhouse sinks near homoclinic tangencies implies that small changes in the parameters may destroy the SA. These observations are reflected in the difficulties of proving the existence of SA in such systems (see reviews [1,4]). Analytical results regarding the existence of SAs [10], their basins of attraction [11], and the construction of unique natural invariant measure [the Sinai-Ruelle-Bowen (SRB) measure] [12] have recently been published for the Hénon map. These proofs are in the strong dissipation limit, for which the SA appears as a one dimensional attractor multiplied by a cantor set. Some of these results may be applied locally to neighborhoods of homoclinic tangencies [13].

It follows that SAs are expected to emerge near homoclinic tangencies. We use analytical tools for locating primary homoclinic tangencies (the Melnikov analysis, [1]) and secondary homoclinic tangencies [the secondary Melnikov function (SMF) [14]]. [Primary homoclinic tangencies are one-loop homoclinic orbits which are  $O(\varepsilon)$  close to the unperturbed homoclinic orbits for  $t \in (-\infty, \infty)$ . Secondary homoclinic tangencies are two-loop homoclinic orbits which are  $O(\varepsilon)$  close to the unperturbed homoclinic orbits for  $t \in (-\infty, t_0], [t_1, \infty)$ , see also Sec. II.] See [15–18] for other works on the subject of multipulse homoclinic orbits in other settings. This presents the first application of the SMF to a dissipative system. Since homoclinic bifurcations are considered an important source of structural instabilities of dynamical systems [19–24], their location in parameter space should indicate regions in which dramatic structural changes appear. Clearly higher-order tangencies exist as well, and finding them all is a useless mission, in particular in view of Newhouse work. The philosophy here is that not all homoclinic tangencies have the same significance: primary tangencies are more important than secondary, secondary more than third order, etc. Thus there is a sense in locating the bifurcation curves of the lower-order homoclinic tangencies. This approach is backed up by the TAM (topological approxima-

\*Electronic address: litvak@wisdom.weizmann.ac.il

†Electronic address: vered@wisdom.weizmann.ac.il

tion method [25,26]), which asserts that many features of the dynamical system are determined already by the characteristics of the primary and secondary homoclinic orbits. The TAM was developed for nondissipative systems and has been recently generalized to dissipative systems [27].

The last part of this work consists of a numerical search for SAs at parameter values which are close to the analytically predicted bifurcation curves. SAs have been observed in various systems exhibiting homoclinic chaos, including the forced and damped Duffing oscillator [1], the Hénon map [23], and the forced and damped cubic potential [28]. In the latter work the correspondence between the appearance of homoclinic tangencies of specific character and SAs has been noted, a correspondence which seems to persist for the AFDO.

This paper is ordered as follows. In Sec. II we present the basic phase space structure of the AFDO, the Melnikov analysis, and the bifurcation curves for primary and secondary homoclinic bifurcations. Numerical evidence suggesting the existence of SAs near specific homoclinic bifurcation curves is presented in Sec. III, as are the typical size and shape of the basins of attraction of the attractors. Conclusions and a discussion are presented in Sec. IV.

## II. TEMPLATES OF THE HOMOCLINIC TANGLE

### A. Basic properties of the AFDO

Introducing the phase space coordinates  $(x,y) \in \mathfrak{R}^2$ , one rewrites Eq. (2) as

$$\dot{x} = y, \quad (3)$$

$$\dot{y} = x - x^3 + (x - \beta x^2) \varepsilon \gamma \cos(\omega t) - \varepsilon \delta y.$$

Physically,  $\delta$  represents the dissipation (the damping),  $\gamma$  the amplitude of the forcing,  $\omega$  the frequency, and  $\beta$  the asymmetry disturbances. These parameters are real and by symmetry may be taken to be non-negative.  $\varepsilon$  is a ‘‘perturbation scaling parameter,’’ assumed to be small. For  $\varepsilon \neq 0$ , there are two differences between the AFDO (2) and the Duffing oscillator (1). The substantial difference is that Eq. (2) includes the asymmetry parameter  $\beta$ . The second difference is that for convenience, with no loss of generality, the symmetry  $x \rightarrow -x, t \rightarrow t + \pi/\omega$  of Eq. (1) is replaced by the symmetry  $x \rightarrow -x$  for  $\beta=0$  in Eq. (2), hence the origin is fixed for all  $\varepsilon, \beta$ .  $\beta \neq 0$  corresponds to symmetry-breaking disturbances.

The unperturbed system corresponds to the integrable Hamiltonian system with a symmetric quartic potential:

$$V(x) = -\frac{x^2}{2} + \frac{x^4}{4}, \quad (4)$$

and with the Hamiltonian function (energy):

$$H(x,y) = \frac{y^2}{2} + V(x) = \frac{y^2}{2} - \frac{x^2}{2} + \frac{x^4}{4}. \quad (5)$$

The unperturbed system, which is identical to that of the unperturbed Duffing oscillator, has three equilibrium points: two centers at  $(x,y) = (\pm 1,0)$ , and a saddle at  $(x,y) = (0,0)$ . The saddle point is connected to itself by two

homoclinic orbits, with periodic orbits nested within and around them. The period of the unperturbed periodic orbits,  $P(H)$ , has the following asymptotic expansion near  $H=0$  (exact formulas for all  $H$  are available [1,4]):

$$P(H) = \begin{cases} \ln(16/-H)[1 + O(H)], & H \rightarrow 0^- \\ 2\ln(16/H)[1 + O(H)], & H \rightarrow 0^+. \end{cases} \quad (6)$$

In the unperturbed system the stable and the unstable manifolds of the saddle point  $(0,0)$  coincide. For  $\delta > 0$ , and  $\gamma = 0$ , the unstable manifold of the saddle point near the origin falls into the two sinks created near  $(\pm 1,0)$ . As for the Duffing oscillator, it may be proved that for sufficiently small values of  $\gamma$  the closure of the unstable manifold (which contains the saddle and the sinks) is an attracting set of Eq. (3).

A Poincaré map in time is used to simplify the phase space portrait for the time dependent system ( $\gamma \neq 0$ ). Keeping  $\delta > 0$ , and increasing  $\gamma$ , the following scenario occurs on both sides of the fixed point; for small values of  $\gamma$ , the Poincaré map is topologically equivalent to the Poincaré map with  $\gamma = 0$ , which is structurally stable. As  $\gamma$  increases, resonance bands of higher period and higher amplitudes are created. As  $\gamma$  is further increased, in addition to the resonances, a homoclinic bifurcation occurs, after which the stable and the unstable manifolds of the saddle point of the Poincaré map intersect in *transversal homoclinic orbits*. The presence of these orbits implies the existence of a complicated non-wandering Cantor set which possesses infinitely many unstable periodic orbits of arbitrary long period as well as bounded nonperiodic motions. The Smale-Birkhoff homoclinic theorem implies that in this case the system has chaotic dynamics. When  $\beta = 0$ , as in the forced Duffing oscillator (1), the sequence of bifurcations described above occurs simultaneously on both sides of the fixed point. When  $\beta > 0$  this changes as described below.

The Melnikov function  $M(t_0 + \theta/\omega)$  measures the signed distance between the stable and the unstable manifolds of a hyperbolic fixed point (up to a multiplication by a constant). This distance is measured at the Poincaré section  $\omega t = \theta$ , and  $t_0$  represents a parametrization along the unstable manifold. For the AFDO [Eq. (3)] two Melnikov functions are defined:  $M_r(t_0; \gamma, \omega, \beta, \delta) \equiv M_r(t_0) [M_l(t_0)]$  measures the signed distance between the right [left] branches of the stable and unstable manifolds. These functions are given by

$$\begin{aligned} M_{r,l}(t_0; \gamma, \omega, \beta, \delta) &= \int_{-\infty}^{\infty} [yx(1 - \beta x) \gamma \cos(\omega t) - \delta y^2] |_{[q^0(t)_{r,l}, t+t_0]} dt \\ &= \gamma \sin(\omega t_0) F_{r,l}(\omega, \beta) - \frac{4}{3} \delta, \end{aligned} \quad (7)$$

where  $q^0(t)_{r,l}$  are the right and left unperturbed homoclinic orbits of the system:

$$q^0(t)_{r,l} = \pm (\sqrt{2} \operatorname{sech} t, -\sqrt{2} \operatorname{sech} t \tanh t), \quad (8)$$

and

$$F_r(\omega, \beta) = [F_1(\omega) - \beta F_2(\omega)], \quad (9)$$

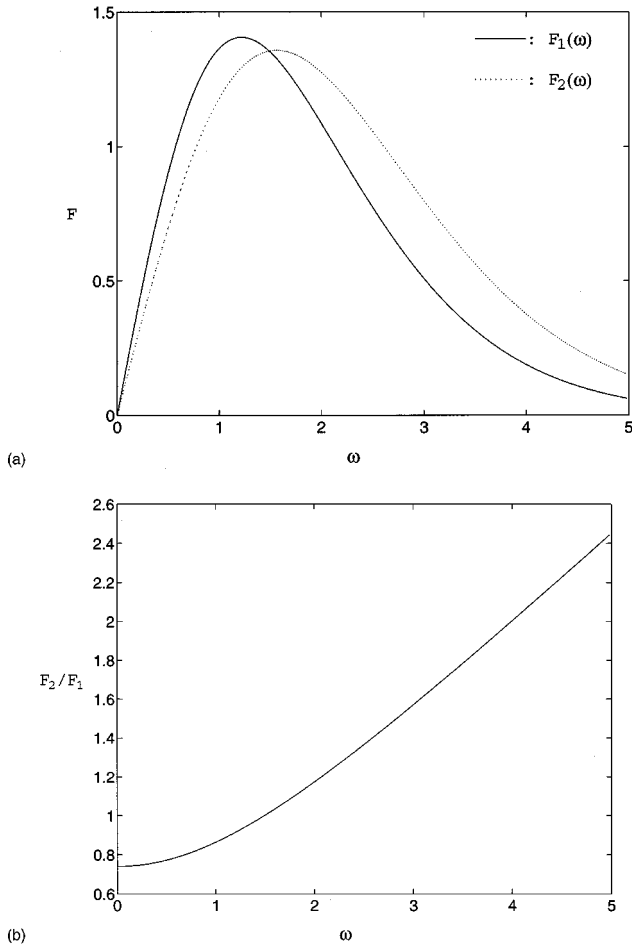


FIG. 1. The Melnikov function amplitude. (a)  $F_1(\omega)$ ,  $F_2(\omega)$ ; (b) the ratio  $F_2(\omega)/F_1(\omega)$ .

$$F_l(\omega, \beta) = [F_1(\omega) + \beta F_2(\omega)], \quad (10)$$

$$F_1(\omega) = \pi \omega^2 \operatorname{csch}\left(\frac{\pi \omega}{2}\right), \quad (11)$$

$$F_2(\omega) = \frac{\sqrt{2}}{3} \pi \omega (1 + \omega^2) \operatorname{sech}\left(\frac{\pi \omega}{2}\right). \quad (12)$$

Figure 1 shows  $F_1(\omega)$ ,  $F_2(\omega)$ , and the relation  $F_2(\omega)/F_1(\omega)$ . Notice that  $F_1(\omega)$  and  $F_2(\omega)$  are non-negative for all  $\omega$ .

### B. Primary homoclinic intersection points

For  $\varepsilon$  sufficiently small simple (degenerate) zeros of the Melnikov function imply primary homoclinic transverse intersections (tangencies) of the stable and the unstable manifolds of the hyperbolic fixed point [1]. Requiring  $M(t_0) = M'(t_0) = 0$ , it follows from Eq. (7) that primary homoclinic bifurcations occur near

$$\begin{aligned} \varepsilon \gamma_{r,l}(\delta; \omega, \beta) &= \varepsilon \delta \left| \frac{4}{3[F_1(\omega) + \beta F_2(\omega)]} \right| \\ &\equiv \varepsilon \delta R_0^\pm(\omega, \beta). \end{aligned} \quad (13)$$

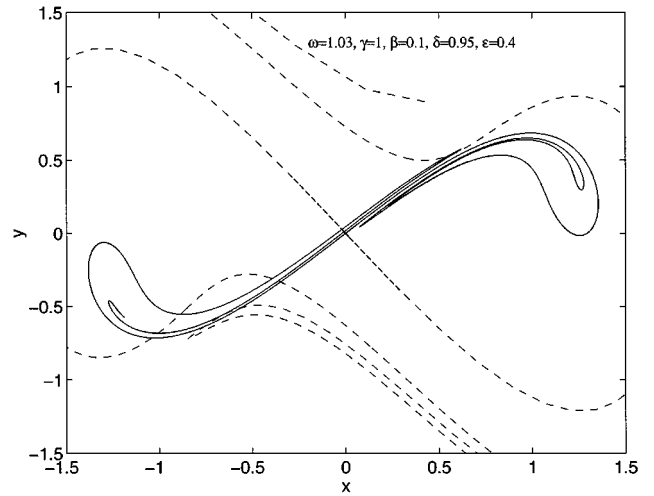


FIG. 2. Intersections of stable and unstable manifolds. ---, stable manifold; —, unstable manifold.

Hence, if

$$\frac{3\gamma|F_1(\omega) - \beta F_2(\omega)|}{4} < \delta \leq \frac{3\gamma[F_1(\omega) + \beta F_2(\omega)]}{4}, \quad (14)$$

then the left branches of the stable and the unstable manifolds intersect, while the right branches do not, see, for example, Fig. 2 (the intersections on the right hand side of this figure correspond to secondary homoclinic points, as described in Sec. II C). Similarly, if

$$\delta \leq \frac{3\gamma|F_1(\omega) - \beta F_2(\omega)|}{4}, \quad (15)$$

then the stable and unstable manifolds intersect on both left and right sides of the hyperbolic fixed point, see, for example, Fig. 7. Schematic phase space portraits are shown in each region.

It follows that the parameter space is divided into three regions (see Figs. 3 and 4).

(I) For  $\gamma/\delta < R_0^-(\omega, \beta)$  there are no primary intersections of the stable and the unstable manifolds.

(II) For  $R_0^-(\omega, \beta) < \gamma/\delta < R_0^+(\omega, \beta)$  the stable and the unstable manifolds have primary intersection points on the left side of the saddle point, and do not have primary intersection points on the right side (asymmetric behavior).

(III) For  $\gamma/\delta > R_0^+(\omega, \beta)$  primary intersections of the stable and the unstable manifolds occur both on the left and the right sides of the saddle point [as in Eq. (1), but in an asymmetric manner for  $\beta \neq 0$ ].

Since

$$\frac{R_0^-(\omega, \beta)}{R_0^+(\omega, \beta)} = \left| \frac{1 - \beta F_2(\omega)/F_1(\omega)}{1 + \beta F_2(\omega)/F_1(\omega)} \right| \equiv r\left(\beta \frac{F_2(\omega)}{F_1(\omega)}\right), \quad (16)$$

the relative size of region II depends on the values of  $x = \beta F_2(\omega)/F_1(\omega)$ , and may be derived from the graph of  $r(x)$  (Fig. 5) for the corresponding  $\beta$  and  $\omega$  values; fixing  $\beta \neq 0$ , the relative size of region II varies with  $\omega$  as described below. First, notice that  $F_2(\omega)/F_1(\omega)$  is bounded from be-

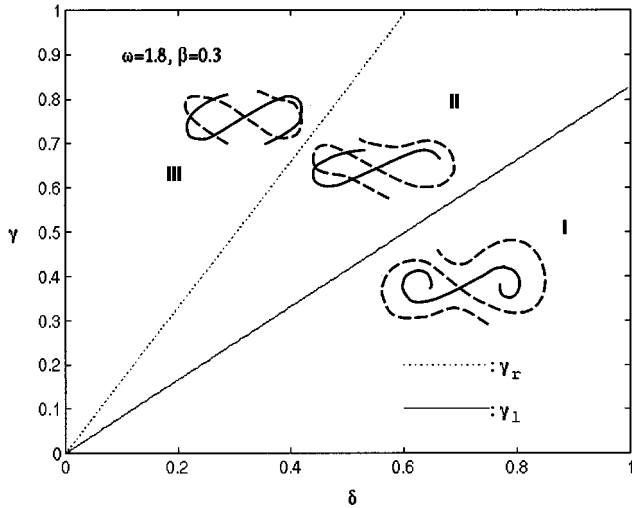


FIG. 3. Primary homoclinic bifurcation curves. Schematic phase space portraits are shown in each region.

low by a positive constant  $c_0 \approx 0.7$ , and that it grows monotonically (in fact asymptotically linearly) with  $\omega$  (see Fig. 1). Therefore, and since  $r(x) = 1$  at  $x = 0, \infty$  only, it follows that for any finite nonvanishing  $\omega$  value region II is of nonvanishing measure (see, for example, Figs. 5 and 4). Since  $x$  grows monotonically with  $\omega$ , and  $x > \beta c_0$ , the relative size of region II increases with  $\omega$  up to the threshold value  $\omega^*(\beta)$  at which  $F_2(\omega^*)/F_1(\omega^*) = 1/\beta$  [i.e.,  $x(\beta, \omega^*(\beta)) = 1$ ]. (If  $\beta > \max_{\omega} [F_1(\omega)/F_2(\omega)] = 1/c_0$ , then  $\omega^*(\beta)$  does not exist, and may be considered as infinite.) For  $x > 1$ ,  $r(x)$  strictly increases with  $x$ , thus for  $\omega > \omega^*(\beta)$  the relative size of region II decreases as  $\omega$  increases. At  $x = 1$ ,  $r(x) = 0$ , namely,  $R_0^+(\omega, \beta) \rightarrow \infty$  as  $\omega \rightarrow \omega^*$ . For these values, regions I and II occupy most of the parameter space, and region III shrinks till it disappears, to order  $\varepsilon$ , at  $\omega = \omega^*(\beta)$ .

**C. Secondary homoclinic intersection points**

First, we describe geometrically the secondary homoclinic intersection points, their transition numbers, and the struc-

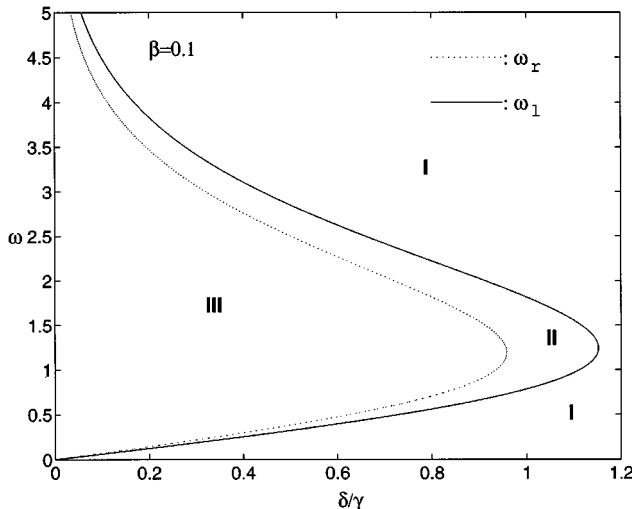
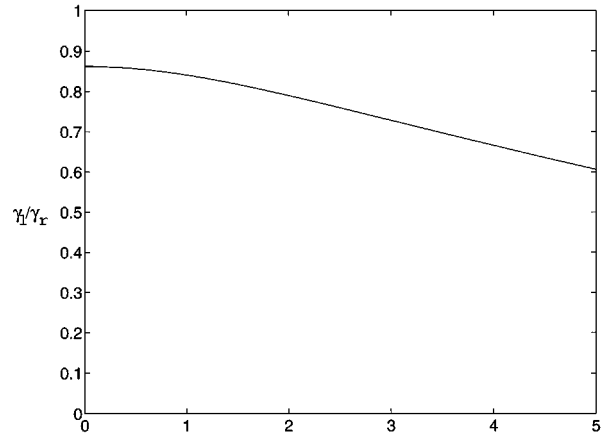
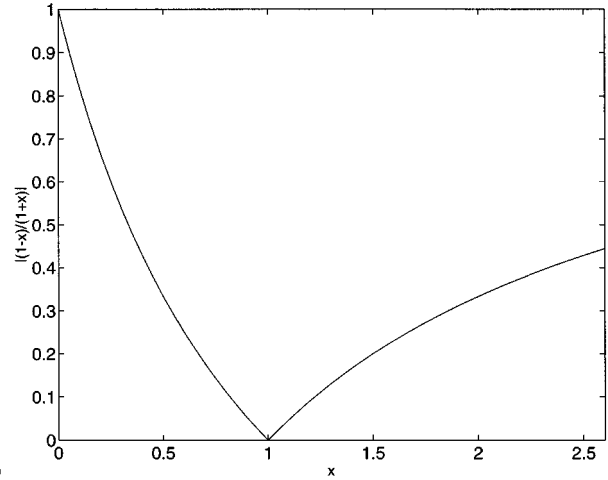


FIG. 4. Primary homoclinic bifurcation curves [in  $(\delta/\gamma, \omega)$  space].



(a)



(b)

FIG. 5. The relative size of region II. (a)  $\gamma_l/\gamma_r(\omega, \beta=0.1)$ , see Eq. (13); (b)  $r(x)$ , see Eq. (16).

tural indices of a homoclinic tangle. Then, we present the analytical (perturbational) method for finding these structural indices.

Consider values of the dissipation parameter  $\delta$  for which the Melnikov function  $M_l(t_0; \mu, \delta)$  [ $M_r(t_0; \mu, \delta)$ ] has two simple zeros (see Sec. II B). Denote the corresponding PIPs (primary homoclinic intersection points), ordered by the direction of the unstable manifold, by  $pl_0$  ( $pr_0$ ) and  $ql_0$  ( $qr_0$ ); see Fig. 6. Also, denote their ordered images under the Poincaré map  $F$  by  $pl_i, ql_i$  ( $pr_i, qr_i$ ),  $i = 0, \pm 1, \pm 2, \pm 3, \dots$ , i.e.,  $F^i(pl_0) = pl_i$  and so on. The areas enclosed by the segments of the stable and the unstable manifolds connecting two successive PIPs are called lobes. Denote the lobes enclosed by segments of the stable and the unstable manifolds connecting  $pl_i, ql_i$  by  $Dl_i$ , and the ones that between  $ql_i, pl_{i+1}$ , by  $El_i$ , when again,  $Dl_i = F^i(Dl_0), El_i = F^i(El_0)$  (the equivalent notation is used for the right side); see Fig. 6.

If  $El_j \cap Dl_k \neq \emptyset$  ( $Er_j \cap Dr_k = \emptyset$ ) for some non-negative integer  $j$ , or if  $Dl_{k+1} \cap Er_0 \neq \emptyset$  ( $Dr_{k+1} \cap El_0 \neq \emptyset$ ) for some non-negative integer  $k$ , then there exist secondary intersection points (SIPs) in these intersections. The integers  $j, k$  are the transition numbers of the corresponding SIPs [29]. The minimal transition numbers (the minimal integers  $j, k$ ) for which this happens on the left side (right side) of the hyper-

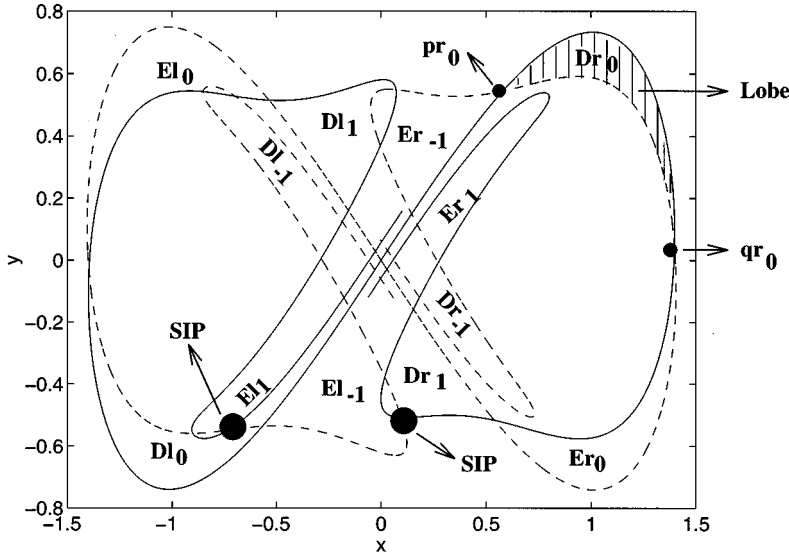


FIG. 6. Illustration of lobes, PIPs, and SIPs. ---, stable manifold; —, unstable manifold.

bollic fixed point are called the structural indices  $\ell_{ll}, \ell_{lr}$  ( $\ell_{rr}, \ell_{rl}$ ) of the homoclinic tangle [29]. Namely, these structural indices are exactly the transition numbers of the secondary homoclinic points which belong to the first intersection of the corresponding lobes. For example, in Fig. 6 the structural indices are  $\ell_{ll}=1, \ell_{lr}=1, \ell_{rl}=1$ , and  $\ell_{rr}=2$ . Each such structural index imposes minimal complexity for the structure of the homoclinic tangle. For example, the length growth rate of line segments along the unstable manifold (the topological entropy) increases as the indices decrease. Thus dividing the parameter space into regions according to the values of these indices corresponds, approximately, to a plot of “level sets” of the topological entropy. The dividing curves correspond to secondary homoclinic bifurcations. Large SAs which are not associated with primary homoclinic tangencies seem to appear only in regions in which at least one structural index is less than or equal to 1 (see also [28]).

The perturbational method for calculating the secondary homoclinic bifurcation curves is described below. For simplicity it is presented specifically for the AFDO model. More generally, it may be applied to nearly Hamiltonian dissipative systems, which satisfy some generic assumptions (see [27]).

Consider the secondary Melnikov function (see [25,26,14,27]):

$$h_2^{cd}(t_0, \varepsilon) = M_c(t_0) + M_d(t_{1cd}(t_0, \varepsilon)),$$

$$c, d \in \{l, r\} \tag{17}$$

where  $M_c(t)$  is the Melnikov function, and  $t_{1cd}$  is defined by

$$t_{1cd}(t_0, \varepsilon) = \begin{cases} t_0 + P(\varepsilon M_c(t_0)), & M_c(t_0) < 0 \\ t_0 + \frac{1}{2} P(\varepsilon M_c(t_0)), & M_c(t_0) > 0 \end{cases} \quad c, d \in \{l, r\} \tag{18}$$

$P(H)$  is the period of the unperturbed periodic orbit with energy  $H$ , and  $H=0$  on the separatrix. For sufficiently small

$\varepsilon$ , simple zeros (degenerate zeros) of Eq. (17) imply transverse secondary homoclinic intersections (tangencies) with a transition number:

$$j_{cd}(t_0, \varepsilon) = \left\lfloor \frac{t_{1cd}(t_0, \varepsilon)}{T} \right\rfloor - s(t_0),$$

$$0 \leq t_0 < T \tag{19}$$

where  $[x]$  is the integer part of  $x$ ,  $T = 2\pi/\omega$  is the period of the perturbation, and  $s(t_0)$  is either 0 or 1, depending on the interval to which  $t_0$  belongs [Eq. (24) below]. The structural index  $\ell_{cd}$  ( $c, d \in \{l, r\}$ ) is defined to be the minimal transition number  $j_{cd}(t_0, \varepsilon)$ . For sufficiently small  $\varepsilon$  this analytical definition of the structural index meets the geometrical definition described above [14]. It follows that typically a change in the structural index may be found at a bifurcation point for Eq. (17). [Another source for changes in the structural indices are points of discontinuity of  $t_1(t_0)$ , see [27].] Indeed, under some generic conditions on  $h_2^{cd}(t_0, \varepsilon; \mu, \delta)$ , the structural indices satisfy [14]

$$\ell_{cd} = j_{cd}(t_{0cd}, \varepsilon_{cd}), \quad c, d \in \{l, r\} \tag{20}$$

where  $(t_{0cd}, \varepsilon_{cd})$  ( $\varepsilon_{cd}$  small) are the solutions to the standard equations for a bifurcation point:

$$h_2^{cd}(t_0, \varepsilon) = 0 \quad 0 \leq t_0 < T \tag{21}$$

$$\frac{\partial h_2^{cd}(t_0, \varepsilon)}{\partial t_0} = 0, \tag{22}$$

defined in the appropriate time interval for  $t_1$ :

$$[\ell_{cd} + s(t_{0cd})]T \leq t_{1cd}(t_{0cd}, \varepsilon_{cd}) < [\ell_{cd} + s(t_{0cd}) + 1]T, \tag{23}$$

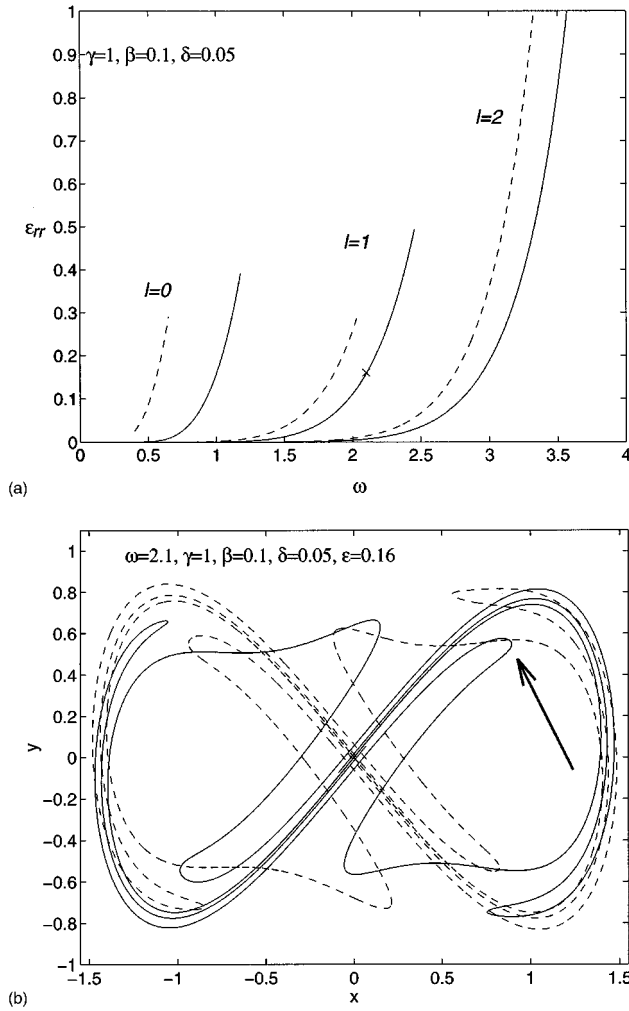


FIG. 7. Secondary homoclinic bifurcation curves and the homoclinic tangle. —,  $\epsilon_{rr}^1$ ; ---,  $\epsilon_{rr}^2$ ; - - -, stable manifold; —, unstable manifold.

$$s(t_{0cd}) = \begin{cases} 0, & t_{0cd} \in \left[0, \frac{T}{2}\right) \\ 1, & t_{0cd} \in \left[\frac{T}{2}, T\right), \end{cases} \quad (24)$$

where  $t_{1cd}(t_0, \epsilon)$  is defined by Eq. (18).

Typically, for  $\epsilon_{cd}$  sufficiently small, one finds a sequence of two bifurcation values,  $\epsilon_{cd}^1 < \epsilon_{cd}^2$ . The corresponding solutions  $(t_{0cd}^i, \epsilon_{cd}^i)$ ,  $i=1,2$  of Eqs. (21) and (22) divide the parameter space into three regions: below the hypersurface  $\epsilon = \epsilon_{cd}^1(\omega, \gamma, \beta, \delta, \ell_{cd})$  there are no SIPs, between the hypersurfaces  $\epsilon = \epsilon_{cd}^1(\omega, \gamma, \beta, \delta, \ell_{cd})$  and  $\epsilon = \epsilon_{cd}^2(\omega, \gamma, \beta, \delta, \ell_{cd})$  two SIPs occur (see, for example, the intersections denoted by an arrow in Fig. 7), and above the hypersurface  $\epsilon = \epsilon_{cd}^2(\omega, \gamma, \beta, \delta, \ell_{cd})$  two additional SIPs occur (see, for example, the intersections of the lobes above the origin in Fig. 7).

Moreover, Eqs. (17)–(22) may be brought to a simple form, as shown in the Appendix. Using the asymptotic expansion for the period function  $P(H)$  [Eq. (6)], these equations may be solved analytically if both  $\beta=0$  and  $\delta=0$ , to

find approximations to the secondary homoclinic bifurcation points  $(t_0^i, \epsilon_{cd}^i(t_0^i))$ ,  $c, d \in \{l, r\}$ ,  $i \in \{1, 2\}$ . The solutions for  $\beta=0$ ,  $\delta=0$  may be used to solve these equations for  $\beta \neq 0$  or/and  $\delta \neq 0$  small by the use of asymptotic expansions in powers of  $\beta$  and  $\delta$  for  $i=1$ , and in powers of  $\beta^{1/3}$  and  $\delta^{1/3}$  for  $i=2$ . To get more accurate results, using  $P(H)$  instead of its approximate form, we use a Newton method, combined with a linear prolongation scheme (see the Appendix and [27] for details). Plotting the bifurcation values,  $\epsilon_{cd}^i(\omega, \gamma, \beta, \delta, \ell_{cd})$ ,  $c, d \in \{l, r\}$ ,  $i \in \{1, 2\}$ , obtained from the solutions to these equations, for  $\gamma, \beta, \delta$  fixed and varying  $\omega$ , gives the secondary homoclinic bifurcation curves in parameter space  $(\omega, \epsilon)$ , labeled by the structural indices,  $\ell_{cd} = 0, 1, 2, \dots, m < \infty$ , as in Fig. 7(a).

A simple lower bound to the homoclinic bifurcation curves [compare with Eq. (A2)] is given by

$$\bar{\epsilon}_{cd}(\omega, \gamma, \beta, \delta, \ell_{cd}) = \begin{cases} \frac{P^{-1}((2\pi/\omega)(\ell_{cd}+1))}{\max_{t_0} |M_c(t_0)|}, & c=d \\ \frac{P^{-1}((4\pi/\omega)(\ell_{cd}+1))}{\max_{t_0} |M_c(t_0)|}, & c \neq d. \end{cases} \quad (25)$$

Therefore, using Eqs. (6) and (7), we find

$$\epsilon_{cd}^{1,2}(\omega, \gamma, \beta, \delta, \ell_{cd}) \geq \frac{16e^{-(2\pi/\omega)(\ell_{cd}+1)}}{\max\{|\gamma F_c - \frac{4}{3}\delta|, |\gamma F_c + \frac{4}{3}\delta|\}}. \quad (26)$$

These give a simple lower bound on the secondary homoclinic bifurcation curves [Note that since the approximation to leading order in  $H$  for the period function  $P(H)$  is used here to calculate  $\bar{\epsilon}_{cd}$ , we get that  $\bar{\epsilon}_{cd} \equiv \bar{\epsilon}_{cc}$  (see the Appendix for more details). Hence the curve  $\bar{\epsilon}_{cc}(\ell_{cc}=n)$  serves as a lower bound to all the eight secondary homoclinic bifurcation curves, related to the structural index  $\ell_{cc}=n$ ,  $\epsilon_{cd}^{1,2}(\ell_{cc}=n)$ , with  $c, d \in \{l, r\}$  and  $n \geq 0$ .] Moreover, geometrically these lower bounds correspond to the values of  $\epsilon$  for which the lobes may get involved in a  $1:(\ell_{cd}+1)$  resonance (see below).

#### Comparison between numerical and analytical results

The analytical method described above for finding the secondary homoclinic bifurcations is of a perturbational nature. Thus, as proved in [14], in the limit of small  $\epsilon$  values it is guaranteed to supply a good approximation to the actual bifurcation value. Here we examine how good an approximation the analytical formulas supply for finite  $\epsilon$  values. Indeed, excellent agreement is achieved between the analytical predictions for the occurrence of SIPs and the numerical calculations of the stable and unstable manifolds for  $\epsilon$  as large as 0.3 and  $\ell_{cd} \geq 1$ ,  $c, d \in \{l, r\}$ , see, for example, Fig. 7. In this figure the  $\times$  at the  $(\omega, \epsilon)$  parameter space indicates the parameter values for which the manifolds, presented in the right figure, are calculated. In the right figure, the corresponding near tangency of the manifolds is indicated by an arrow. In fact, the larger the  $l$ 's, the larger the  $\epsilon$  values for which the zeroth-order approximation is found to be adequate. For example, for  $\ell=2$  we find excellent agreement

up to  $\varepsilon \approx 1$ . This is not surprising since large  $l$ 's (and finite  $\varepsilon$ ) correspond to large  $\omega$ 's for which the Melnikov function coefficient becomes exponentially small, thus the effective perturbation is small.

For  $\ell_{cc} = 0$  the agreement between the numerical and the analytical results is not as favorable (notice that this is a finite  $\varepsilon$  effect: letting  $\varepsilon \rightarrow 0$ , with all other parameters held fixed, necessarily implies that  $\ell \rightarrow \infty$ ). This is due to the passage of the manifolds through a 1:1 resonance relation between the periodic orbits inside the homoclinic loop and the forcing period  $2\pi/\omega$ ; namely, the energy level to which the manifolds are pushed by the Melnikov function is near the energy level for which a 1:1 resonance occurs. (Indeed, the  $1:m$  resonance relation for the periodic orbits of Eq. (3) is given by  $P(H) = 2\pi m/\omega$ . Since by definition of  $t_{1cc}$  [see Eq. (18)],  $P(\varepsilon_{cc} M_c(t_{0cc})) = t_{1cc} - t_{0cc}$ , and by condition (23),  $t_{1cc} - t_{0cc} \in (\ell_{cc}(2\pi/\omega), \{\ell_{cc} + 1\}(2\pi/\omega))$ , the manifolds “pass” through the 1:1 resonance zone for  $\ell_{cc} = 0$ .) Now, the construction of the SMF uses the Whisker map (see [30,29,31,32,25,26,14,33]) in which the motion of the interior orbits is approximated by unperturbed periodic motion. This approximation fails near a 1:1 resonance. Hence the analytical approximation for the  $\ell_{cc} = 0$  bifurcation curve is inaccurate even for small values of  $\varepsilon$ . Notice that in this limit  $\omega$  is varied with  $\varepsilon$ , hence this observation is not contradictory to the SMF theorems which hold in the limit  $\varepsilon \rightarrow 0$  with all other parameters held fixed [14]. Indeed, to avoid passage of the manifolds through a 1:1 resonance,  $\varepsilon$  should satisfy the condition  $\varepsilon_{cc} < P^{-1}(2\pi/\omega)/M_c(t_{0cc})$ . This condition holds for  $\ell_{cc} \geq 1$ . For the outer indices  $\ell_{cd}$ ,  $c \neq d$  the problem of 1:1 resonance was not encountered.

### III. STRANGE ATTRACTORS

In this section numerical evidence for the existence of SAs, and observations regarding their location in parameter space and their structural properties in phase space are presented.

#### A. Numerical scheme for detecting SAs

Simple numerical experiments showing Poincaré maps of the AFDO (using DSTOOLS [34]) suggested that SAs appear in the area of the parameter space related to the structural indices  $\ell_{cd} = 0$ ,  $c, d \in \{l, r\}$ . To investigate this subject more thoroughly the Lyapunov exponents of orbits of Eq. (3) were computed (see [35]). Viewing Eq. (3) as an autonomous system, each orbit has three Lyapunov exponents, one zero, one negative, and the third may be either positive or negative. A positive third Lyapunov exponent indicates the existence of a strange attractor (see [9]), while a negative third Lyapunov exponent indicates that the orbit is attracted to a periodic sink.

An efficient stopping criteria for the Lyapunov exponents calculation is developed, using the distinction between SAs or sinks with long transients and simple sinks. First, to remove transient behavior,  $N_{in}$  iterations of the Poincaré map ( $N_{in} = 200$  was found sufficient) are calculated. Then, every  $N_{it}$  iterations ( $N_{it} = 100$ ) a line is fitted to the logarithm of

the modulus of the last  $N_{it}$  Lyapunov exponent values. The program stops if one of the following events occurs

- (1) The largest Lyapunov exponent is negative. Then there exists a periodic sink. The exact value of the negative Lyapunov exponent is not sought.

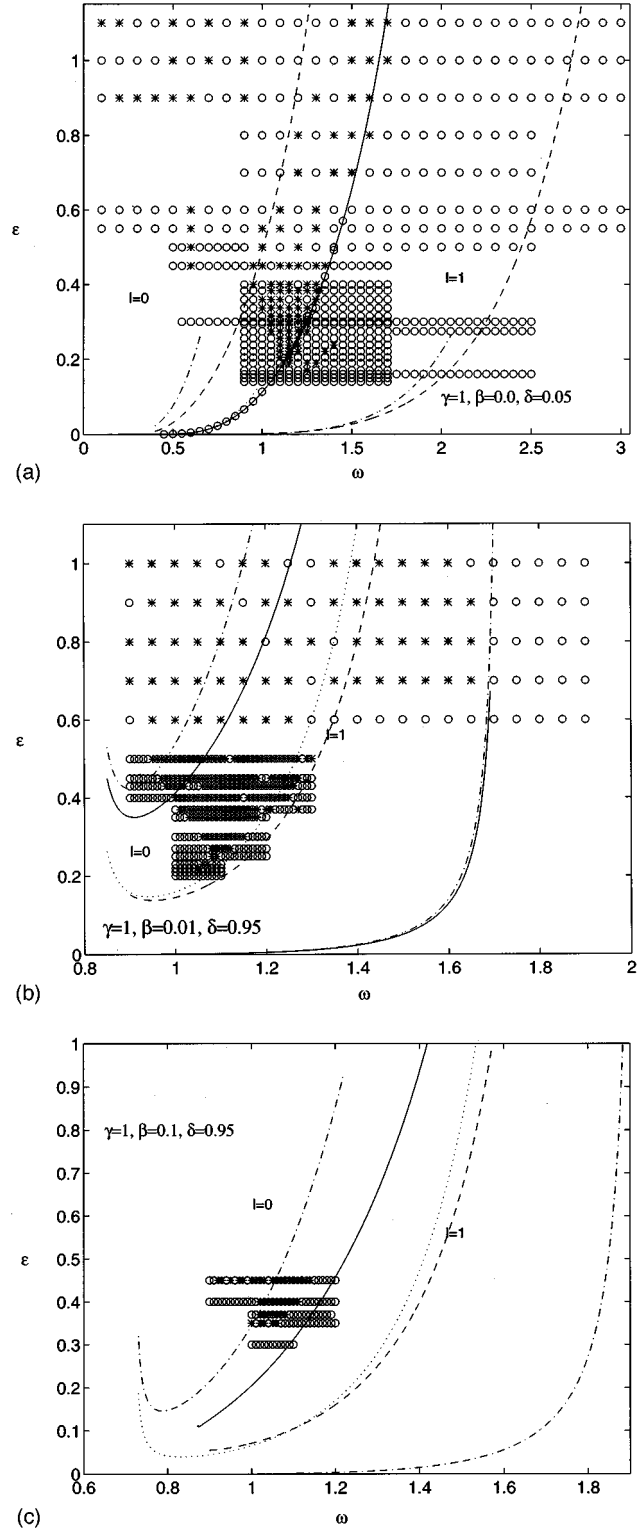


FIG. 8. Secondary homoclinic bifurcation curves and SAs, \*, a SA (positive Lyapunov exponents);  $\circ$ , a periodic orbit (negative Lyapunov exponent); —,  $\varepsilon_{lr}^1$ ; ---,  $\varepsilon_{lr}^2$ ; ····,  $\varepsilon_{ll}^1$ ; - · - ·,  $\varepsilon_{ll}^2$ . (a)  $\beta = 0$ ,  $\delta = 0.05$ . (b)  $\beta = 0.01$ ,  $\delta = 0.95$ . (c)  $\beta = 0.1$ ,  $\delta = 0.95$ .

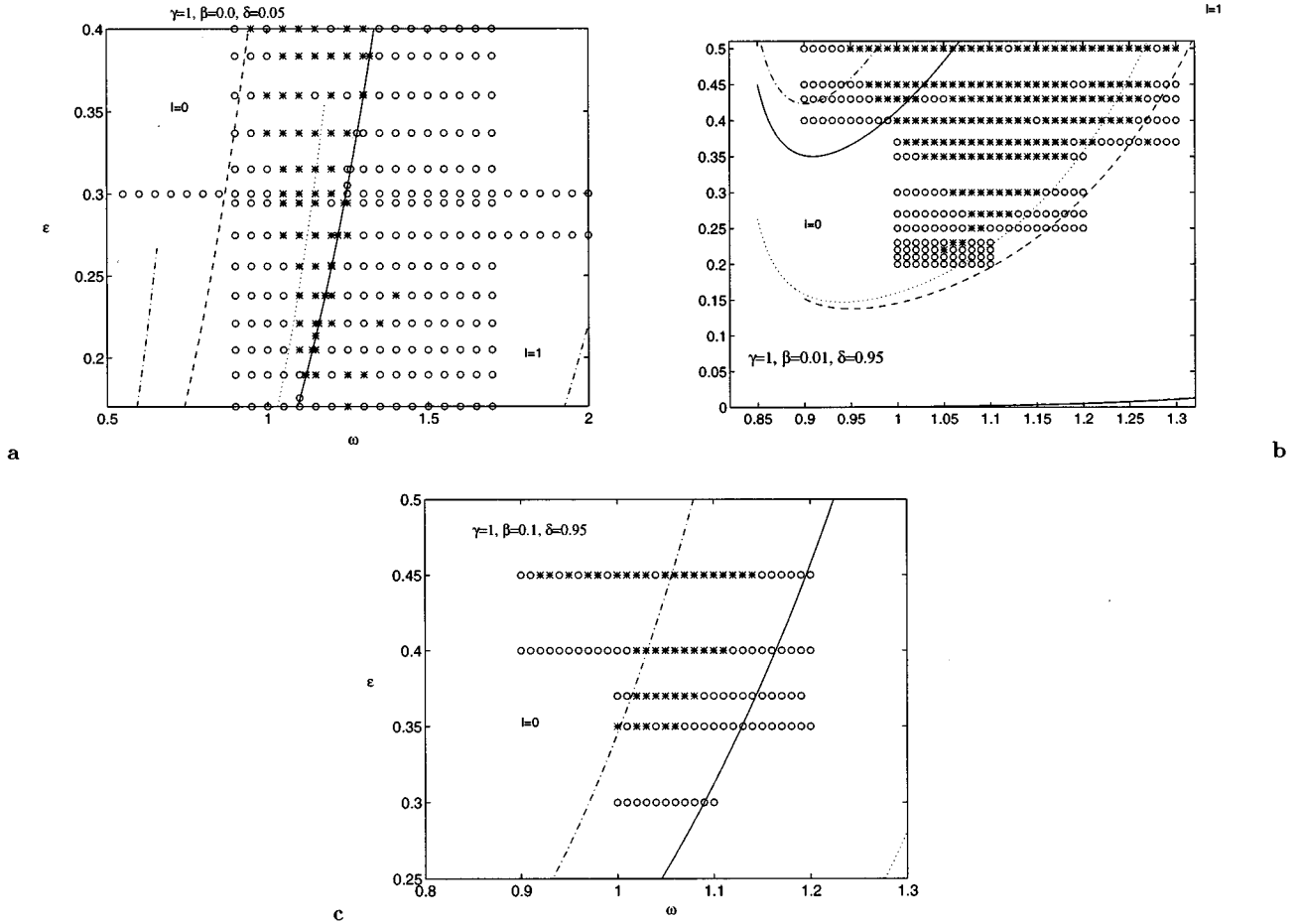


FIG. 9. Secondary homoclinic bifurcation curves and SAs: Magnification of certain regions of Figs. 8(a)–8(c).

(2) The largest Lyapunov exponent is positive and the slope of the fitted line is nearly zero (up to an error of  $1e-6$ ).

(3) The total number of Poincaré map iterations exceeds 10 000. In this case no decision is made regarding the existence or nonexistence of an attractor. In practice the stopping criteria (1) and (2) occur before 10 000 iterates are computed.

In case (2), when a positive Lyapunov exponent is detected, all the Lyapunov exponents are calculated. Hence the Lyapunov dimension [36] of the SA may be calculated. Note that the Lyapunov dimension  $D_L$  is an upper limit for the capacity (or box-counting) dimension  $D_0$  [36].

In the numerical experiments,  $\gamma, \beta, \delta$  are fixed and  $\varepsilon$  and  $\omega$  are varied along and near the secondary homoclinic bifurcation curves  $\varepsilon_{cd}^i(\omega, \gamma, \beta, \delta, \ell_{cd})$ ,  $i=1,2$ ,  $c,d \in \{l,r\}$ , of Sec. II C.

### B. Windows of SA

For various parameter values, numerical evidence suggests the existence of SAs in “windows” in the parameter space. These windows are aligned near the secondary homoclinic bifurcation curves which are related to the structural indices  $\ell_{ll}, \ell_{lr}=0$ , see Fig. 8, and the magnification of the windows in Fig. 9. (Notice that in Fig. 8(a)  $\beta=0$  hence  $\varepsilon_{ll}^i \equiv \varepsilon_{rr}^i$  and  $\varepsilon_{lr}^i \equiv \varepsilon_{rl}^i$ , whereas in Fig. 8(b)  $\varepsilon_{ll}^i \neq 0 \varepsilon_{rr}^i$  and  $\varepsilon_{lr}^i \neq \varepsilon_{rl}^i$ , but, for clarity,  $\varepsilon_{rr}^i, \varepsilon_{rl}^i$  are not plotted. In Fig. 8(c)

$\varepsilon_{rr}^i, \varepsilon_{rl}^i$  are not defined for the specified  $\omega$  values [since the Melnikov function  $M_r(t_0)$  has no zeros].) While theoretically such regions should appear near all tangent bifurcations with arbitrary  $\ell$ , we did not detect in our numerical search any SAs near the bifurcation curves with  $\ell > 0$ . This suggests that the size of the parameter regions for which SAs appear decreases dramatically with  $\ell$ .

In fact, our perturbational methods for detecting the homoclinic tangencies associated with the structural indices  $\ell_{ll}=0$  are inaccurate, see Sec. II C. Nonetheless, the predicted analytical bifurcation curves for  $\ell_{cd}=0$ ,  $c,d \in \{l,r\}$  still lie in the area of parameter space near which the actual bifurcation curves exist. Moreover, we observe that the SAs appear only in the region of the parameter space  $(\omega, \varepsilon)$ , which is above the second secondary bifurcation curve  $\varepsilon_{ll}^2(\omega, \gamma, \beta, \delta, \ell_{ll}=1)$  (see Sec. II C). For  $\varepsilon < 1$ , our predictions for this curve are accurate, hence this curve may be considered as a lower bound to the region in parameter space in which SAs appear, see Fig. 8.

Another feature of the windows of SAs is that they all seem to appear above a threshold value  $\tilde{\varepsilon}(\omega, \gamma, \beta, \delta) \geq 0.2$ . Namely, they do not seem to extend to the small  $\varepsilon$  values to which some of the  $\ell=0$  bifurcation curves extend. Numerical calculations of the stable and the unstable manifolds of the origin for the minimal  $\varepsilon$  values for which SAs are found suggest that this curve is a specific homoclinic bifurcation curve; above this curve the lobe  $El_1$  intersects the lobe  $Dl_0$

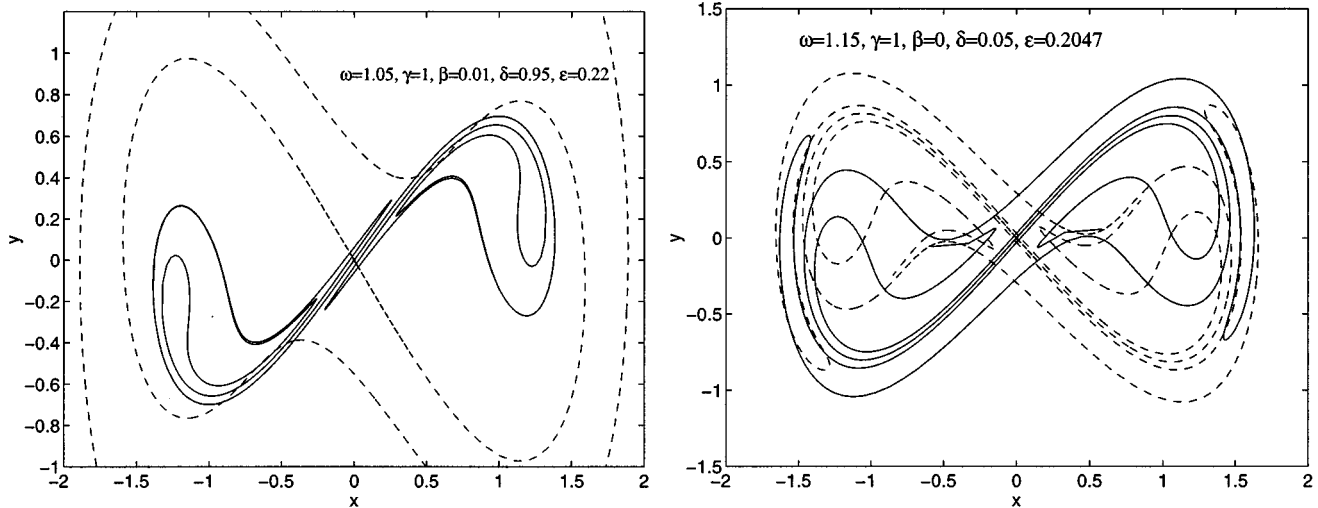


FIG. 10. The stable and the unstable manifolds corresponding to SA. ---, stable manifold; —, unstable manifold.

at five or more (six, seven, or eight) homoclinic intersection points. See, for example, Fig. 10. Notice that the homoclinic bifurcation curve  $\varepsilon_{II}^2(\omega, \gamma, \beta, \delta, \ell_{II}=1)$  in the  $(\omega, \varepsilon)$  parameter space gives a lower bound to this curve.

The structures of the SAs that are obtained vary with the parameters. The main forms of the attractors which were found are described next.

### C. The phase space structure of the SAs

The observed SAs have the following two distinct properties.

(1) The attractors may be one sided (i.e., the attractor is contained in the right or left half phase space plane) or two sided (with one or two components).

(2) The attractors may have strong dissipative features or may have nearly conservative features.

The first property depends on the location of the parameter values with respect to the division into regions I, II, and III. One-sided SAs may appear in region II near secondary homoclinic bifurcations or near the borders between the regions, namely, near primary homoclinic tangencies, see Fig. 11. There, the transition between two-sided SAs, denoted by  $T$ , and one-sided SAs, denoted by  $O$ , is shown. (This transition is not continuous in  $\delta/\gamma$ ; between the value of  $\delta/\gamma$  for which a two-sided SA appears, and the value of  $\delta/\gamma$  for which a one-sided SA appears, there may be some values of  $\delta/\gamma$  for which no SAs appear.) In fact, near the border between regions II and III three different SAs may appear: a one-sided SA on the right half plane, two one-sided SAs or a two-sided SA. Near the border between regions I and II left sided SAs, coexisting with a sink on the right half plane, were observed.

The second property seems to depend mainly on the ratio  $\delta/\gamma$  and is roughly independent of the other parameters (in regions where SAs exist); this is somewhat surprising since the area contraction per Poincaré map is given by  $\exp(-\varepsilon \delta 2\pi/\omega)$ —thus strong dissipation may be achieved for fixed  $\delta/\gamma$  by increase of  $\varepsilon$ , without essential changes in the structure of the SA. For  $\delta/\gamma \ll 1$ , the two-sided SA seems to have nearly conservative features of a chaotic region, see

Fig. 12. These features persist in the window shown in Fig. 9(a), and even when  $\varepsilon = 1$ , though the attractor is more structured, it has “fat” regions in which no filamentation is observed. The positive Lyapunov exponent corresponding to this figure is  $\log_2(\alpha_1) \approx 0.1987$ , and the corresponding Lyapunov dimension is  $D_L \approx 1.9036$ . The SAs indicated in Fig. 8(a) are of such structure. Most of these attractors have a positive Lyapunov exponent of about 0.2. The maximal observed deviation from this value is 0.02. Nearly conservative one-sided SAs were not observed.

When  $\delta/\gamma$  is not small ( $\delta/\gamma = 0.2$  is already in this region), the structure of the SA is associated with the folding of the unstable manifold as in strongly dissipative systems, see Fig. 13. The corresponding positive Lyapunov exponent is  $\log_2(\alpha_1) \approx 0.1741$ , and the Lyapunov dimension is  $D_L \approx 1.2975$ . Comparing with the above results for the nearly conservative attractors, we observe that the Lyapunov exponent is less sensitive to the attractor’s structure than the Lyapunov dimension. The SAs indicated in Fig. 9(b) are of strongly dissipative nature; some are two sided with a positive Lyapunov exponent very close to 0.17, with maximal deviation of 0.03, and some are one sided.

In Fig. 14 such a one-sided SA is shown; its positive Lyapunov exponent is  $\log_2(\alpha_1) \approx 0.0862$ , and its Lyapunov dimension is  $D_L \approx 1.1453$ . The SAs presented in Fig. 8(c) are all one-sided strongly dissipative (Hénon-like) SAs. The values of the positive Lyapunov exponent are  $0.08 \pm 0.04$ , about half of the Lyapunov exponents of the two-sided SA.

The Lyapunov exponent and dimension of the attractors seems to be quite robust. The dependence of the Lyapunov exponents on the values of  $\varepsilon$  along a secondary homoclinic bifurcation curve related to a structural index  $\ell_{cd} = 0$  is shown in Fig. 15. An example for the dependence of the Lyapunov dimensions on the values of  $\varepsilon$  along such a bifurcation curve is shown in Fig. 16. The plunges in the figure correspond to parameter values for which no SAs exist.

In [27] symbolic dynamics of segments of the unstable manifold is constructed for the AFDO, and for general dissipative systems which unfold homoclinic tangencies. From this symbolic dynamics a transfer matrix may be constructed

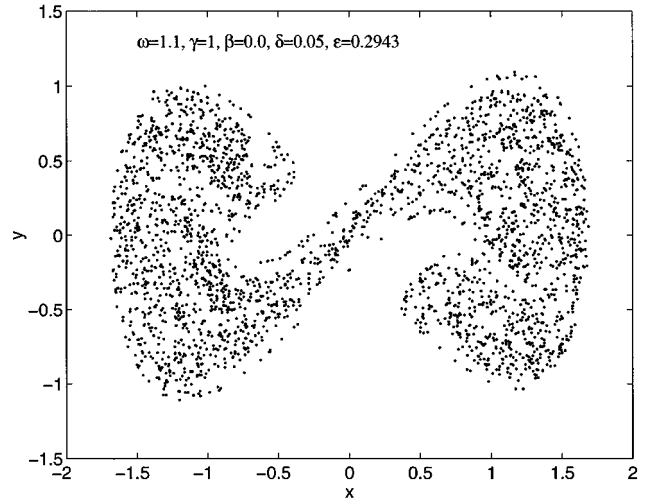
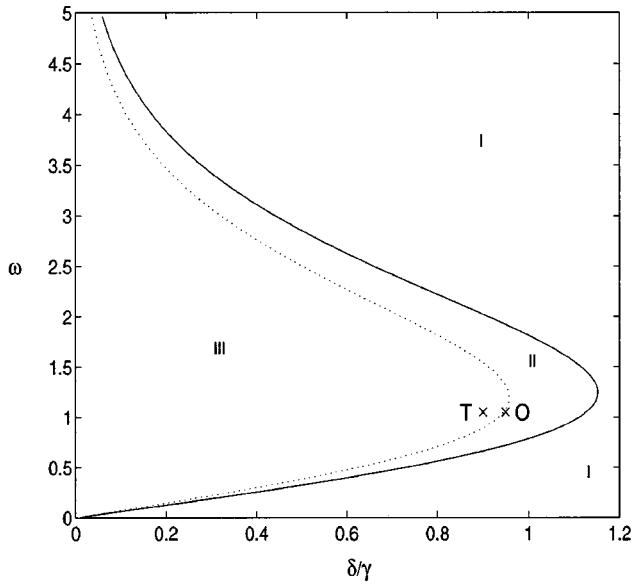


FIG. 12. Nearly conservative SA.

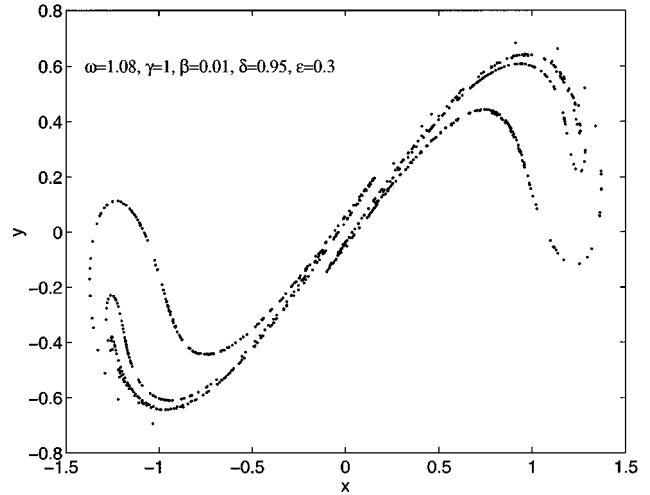
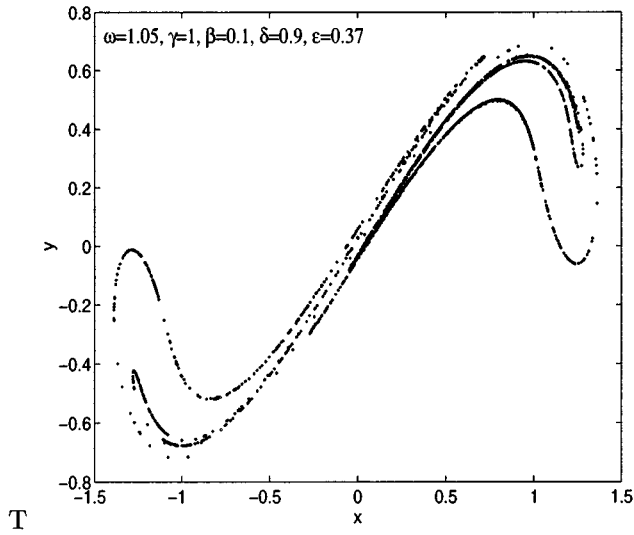


FIG. 13. Two-sided SA with structure referring to large values of the relation  $\delta/\gamma$ .

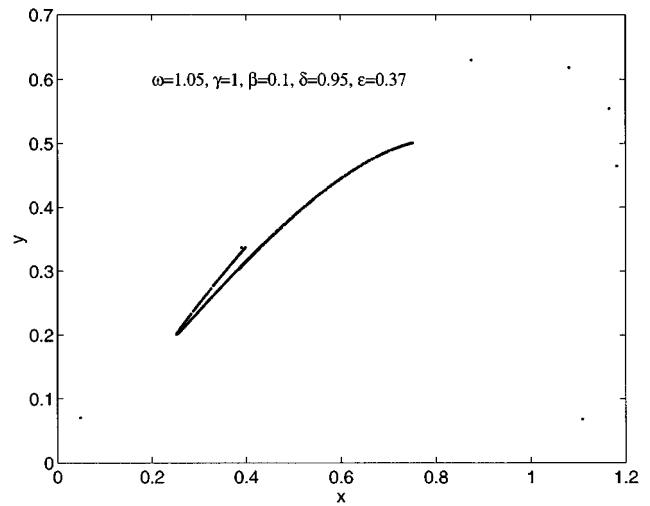
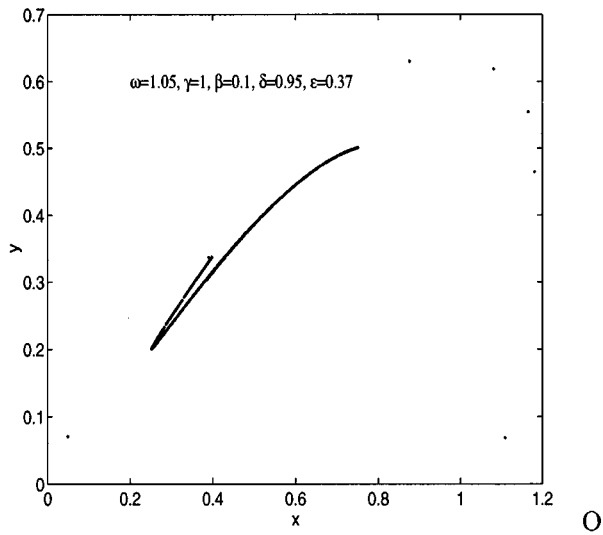


FIG. 11. Transition from two-sided to one-sided SA.

FIG. 14. One-sided SA.

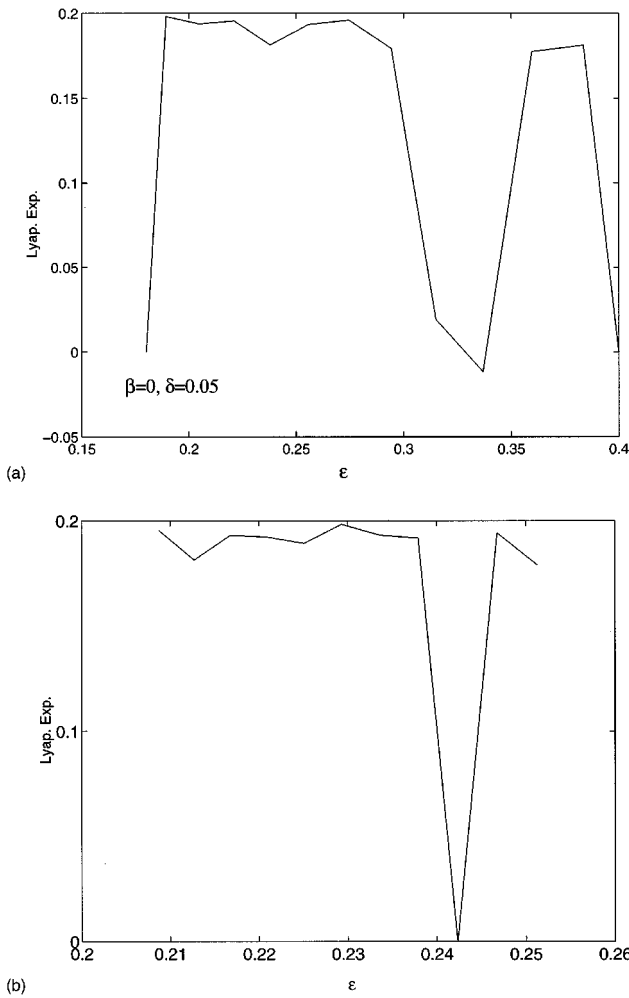


FIG. 15. The positive Lyapunov exponent variation.  $\beta=0$ ,  $\delta/\gamma=0.05$ , and  $l_{lr}=0$ . (a) Samples of  $\epsilon$  values along the bifurcation curve  $\epsilon = \epsilon_{lr}^1(\omega, \gamma, \beta, \delta, l_{lr})$ . (b) Zoom in on  $\epsilon$  values in the interval  $[0.2, 0.25]$ .

for each set of the structural indices  $\mathcal{L}_{cd}$ ,  $c, d \in \{l, r\}$ . It follows from [37,26] that  $\log_2(\lambda)$ , where  $\lambda$  is the modulus of the largest eigenvalue of the transfer matrix, gives a lower bound on the topological entropy of the Poincaré map. The lower bound on the topological entropy for the AFDO with  $\mathcal{L}_{cd}=0$ ,  $c, d \in \{l, r\}$ , corresponding to the region in parameter space where two-sided SAs appear, is  $\log_2(3.9231) = 1.9720$ . The lower bound on the topological entropy for the AFDO, corresponding to the existence of one-sided SAs is  $\log_2(3.6709) = 1.8761$ .

The above results are consistent with the inequalities describing the relations between topological entropy, entropy (Kolmogorov-Sinai invariant), and positive Lyapunov exponents (see [9,38]):

$$h(\rho) \leq h_{\text{top}},$$

$$h(\rho) \leq \sum_{\lambda_i > 0} \lambda_i,$$

where  $\rho$  is an ergodic measure with compact support, with respect to a diffeomorphic map  $F$ , and  $\lambda_i$  are the positive

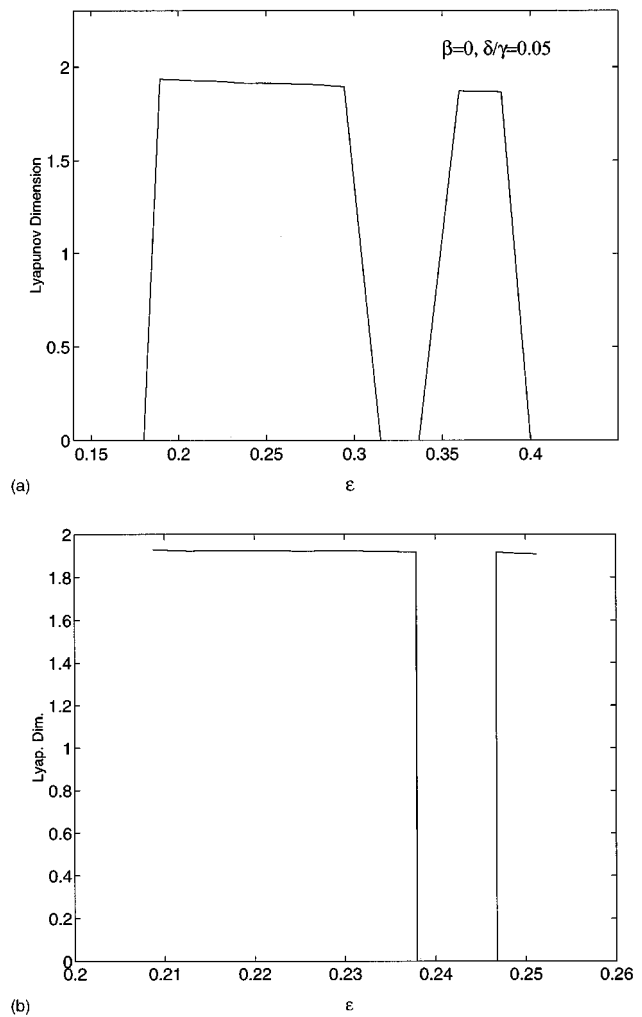


FIG. 16. The Lyapunov dimension variation.  $\beta=0$ ,  $\delta/\gamma=0.05$ , and  $l_{lr}=0$ . (a) Samples of  $\epsilon$  values along the bifurcation curve  $\epsilon = \epsilon_{lr}^1(\omega, \gamma, \beta, \delta, l_{lr})$ . (b) Zoom in on  $\epsilon$  values in the interval  $[0.2, 0.25]$ .

Lyapunov exponents corresponding to a dense orbit of  $F$ , i.e., for the structural indices  $\mathcal{L}_{cd}=0$  we get

$$h(\rho) \leq \lambda_1 \approx \log_2(\alpha_1) < \log_2(\lambda) \leq h_{\text{top}}.$$

Notice that the lower bounds obtained for the topological entropy are larger by an order of magnitude than the corresponding Lyapunov exponents and that there is very little difference between the one-sided and the two-sided cases. See [25,27] for the construction of the symbolic dynamics of the lobes, and details on how the transfer matrices and the lower bounds on the topological entropy may be calculated.

#### D. Basins of attraction

Initial conditions may be attracted to the various attractors which exist in the phase space. Here, we distinguish between three types of attractors: those located entirely on the left (right) half plane and those which are located on both sides of the  $y$  axis. We do not distinguish here between the basins of attraction of different sinks or SAs, see [24,39–41,28] for detailed study of these issues.

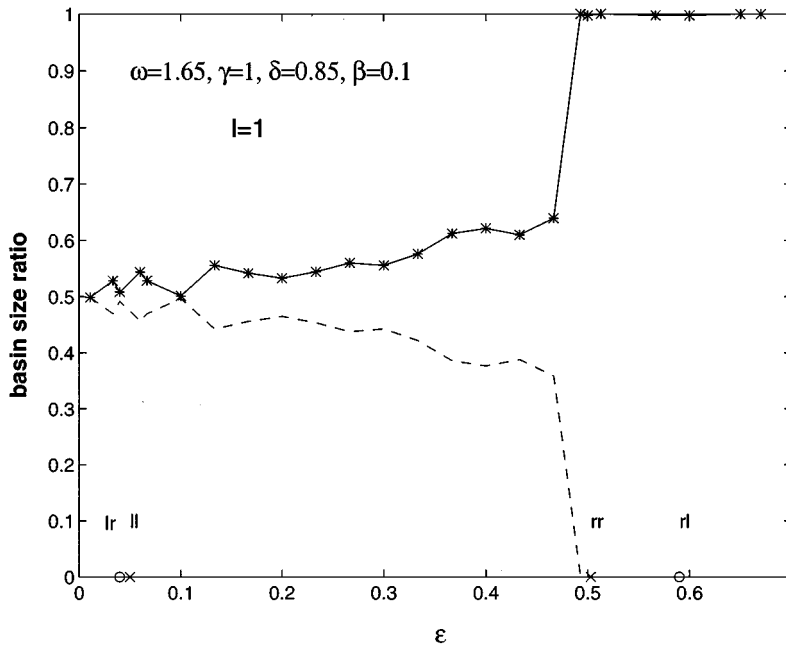


FIG. 17. The relative size of the right and left basins of attraction. —, the right basin size; ---, the left basin size; \*, sampled values of  $\epsilon$ . The secondary homoclinic bifurcation values  $\epsilon(l_{cc}=1)$  are denoted by  $\times$  and the secondary homoclinic bifurcation values  $\epsilon(l_{cd}=1)$  are denoted by  $\circ$ .

The flux of phase space area into the left or right sides may be calculated to first order in  $\epsilon$  by integrating the Melnikov function:

$$\Delta_{l,r}^{in} = \int_0^{s_0} M_{l,r}(s) ds + \int_{s_1}^T M_{l,r}(s) ds = \begin{cases} -\frac{8\pi\delta}{3\omega}, & s_0 = s_1, \quad M_{l,r}(s) < 0 \quad \forall s \in [0, T] \\ -\frac{2\gamma}{\omega} F_{l,r} \left[ 1 - \left( \frac{4\delta}{3\gamma F_{l,r}} \right)^2 \right]^{1/2} - \frac{4\delta}{3\omega} \left[ 2\arcsin\left( \frac{4\delta}{3\gamma F_{l,r}} \right) + \pi \right], & s_0 \neq s_1 \end{cases} \quad (27)$$

$$s_0 = \frac{1}{\omega} \arcsin\left( \frac{4\delta}{3\gamma F_{l,r}} \right), \quad s_1 = \frac{\pi}{\omega} - s_0,$$

where  $s_0, s_1$  are determined by  $M_{l,r}(s) \leq 0$  for  $s_0 \leq s \leq s_1 \in [0, T]$ . Thus on the  $n$ th iterate the initial phase space area,  $|\Delta_{l,r}^{in}| \exp(2\pi\epsilon\delta n/\omega)$ , is swept into the left or right side. In region I,  $M_{l,r}(s) < 0 \forall s \in [0, T]$ , and  $|\Delta_r^{in}| = |\Delta_l^{in}|$  to order  $\epsilon$ . Since  $F_r < F_l$  it can be easily shown that  $|\Delta_r^{in}| > |\Delta_l^{in}|$  in regions II and III. Thus for parameter values corresponding to these regions the influx to the right side is always larger than the influx to the left side (recall that  $\beta > 0$ ).

If  $M_{l,r}(s)$  has simple zeros (so  $s_0 \neq s_1$ ) then, similarly, the flux out of the left or right sides is given by

$$\Delta_{l,r}^{out} = \int_{s_0}^{s_1} M_{l,r}(s) ds = \frac{2}{\omega} \left\{ \gamma F_{l,r} \left[ 1 - \left( \frac{4\delta}{3\gamma F_{l,r}} \right)^2 \right]^{1/2} + \frac{4\delta}{3} \arcsin\left( \frac{4\delta}{3\gamma F_{l,r}} \right) - \frac{2\pi\delta}{3} \right\}. \quad (28)$$

In region II,  $\Delta_r^{out} = 0$ , hence obviously  $|\Delta_l^{out}| \geq |\Delta_r^{out}|$  in this region, and it can be shown that  $|\Delta_l^{out}| \geq |\Delta_r^{out}|$  in region III as well (i.e., for  $\delta \leq 3\gamma F_r/4$ ).

One might expect that the ratio between the fluxes to the right and left regions determines the ratio between the sizes of the basins of attraction. However, in regions II and III

near the borderline between the regions, this picture may change dramatically; there are cases for which all the initial conditions which are numerically integrated are attracted to the right side.

Numerical calculations of the basins of attraction of the left or right attractors suggest a more detailed description.

(1) No intersections on both sides — region I: To order  $\epsilon$ , by Eq. (27) the left and right influx areas are equal, but high-order terms alter these results. Indeed, numerically it is found that the right basin is larger than the left one. Moreover, its area seems to grow monotonically as  $\delta$  decreases to its threshold value,  $3\gamma F_l/4$ .

(2) Intersections on the left side or on both sides—regions II and III: As  $\delta$  is further decreased, the area of the right basin continues to grow. However, the growth in the basin's area seems to be discontinuous. This phenomenon is associated with the “boundary metamorphosis” [41] of the subharmonics. For some parameter values in region III a *two-sided* periodic orbit or a SA may exist, hence in these cases, some (or most) of the initial conditions are attracted neither to a left nor to a right attractor.

There seems to be a correlation between the discontinuities and the occurrence of homoclinic tangencies. See, for example, Fig. 17. In this figure the percentage of the sampled

phase space area which is swept to the left or right side, up to an approximated error of  $\pm 0.03$ , is presented as a function of  $\varepsilon$  (all the other parameters are fixed), where the values of  $\varepsilon$  which correspond to secondary homoclinic bifurcation curves are specified. The results of this figure are somewhat puzzling; one would expect that left or right attractors are composed, for  $\ell \geq 0$ , from the attracting resonances. Hence, when the unstable manifold intersects through the resonance region, it depletes the resonance, thus decreasing the relative area of the basin of attraction of the corresponding side. However, in Fig. 17, along with results that confirm this scenario (see, for example, the jump near  $\varepsilon = 0.06$ ), we observe quite the contrary results (see, for example, the huge jump near  $\varepsilon = 0.5$ ). Possibly other, undetected bifurcation is responsible for these results.

In [28], numerical results regarding the relation between homoclinic and other bifurcation curves and the basins of attraction of systems with a cubiclike potential well are presented. There, it has been suggested that the bifurcation curve, corresponding to what we call here a secondary homoclinic bifurcation curve with a structural index  $\ell = 0$ , is of great significance, since closely beneath it they numerically observed a chaotic escape (i.e., a destruction of the basin of attraction of the SA). Their chaotic escape corresponds, in a case of a *closed* system, to a decrease in the basin of attraction of one side and an increase in the basin of attraction of the other side. (A system is called *closed* if some forward iteration of the Poincaré map of a segment of the unstable manifold which has left the left or right region returns to it. See [27] for a more precise definition.) Thus the current results are in agreement with the results obtained in [28] for *open* systems. Possibly, the critical curves (near which SAs appear or lose stability) that they have observed numerically correspond to the curves discussed above: the homoclinic bifurcation curve above which the lobe  $El_1$  intersects the lobe  $Dl_0$  at least five points, and the curve at which the unstable manifold intersects the resonance region.

**IV. DISCUSSION AND CONCLUSIONS**

The qualitative differences between the flows under symmetric and asymmetric forcing loom when primary homoclinic intersections or tangencies occur only on one side of the saddle fixed point (region II plus its neighborhood). This region may be of significant size even for very small asymmetry values ( $\beta \ll 1$ ) if the forcing frequency is appropriately set. It is of negligible size in the adiabatic limit, hence, to the best of our knowledge, was not observed in previous works which have considered asymmetric potentials with adiabatic forcing. In this fat region II, the system may possess one one-sided SA (strange attractors), two one-sided SAs, or one two-sided SA. In the former case the attractor may be situated on either side of the fixed point; however, the nature of the basin of attraction of the left and right SAs seems to be different.

We find that the relative size of the basin of attraction to the left or right attractors is usually not sensitive to its strangeness (i.e., the size of the basin does not change significantly when a SA is destroyed or created). In general, the basin of attraction of the right attractor is always a bit larger than that of the left attractor, where in most cases the differ-

ence between the fluxes to the right and left regions determines the ratio between the sizes of the basins of attraction. This occurs in a continuous and natural way in region I, however, near the border between regions II and III, where one-sided SA may appear (on either side of it), this picture may change dramatically; there are cases for which all the initial conditions which are numerically integrated are attracted to the right side.

The robust, observable (hence physically significant) SAs appear near primary homoclinic tangencies and near secondary homoclinic tangencies with small structural index. A key perturbational tool for finding the latter is the SMF [14]. Generally, it is found that the SMF supplies excellent analytical prediction to the occurrence of secondary homoclinic tangencies even for relatively large values of  $\varepsilon$ . However, it fails near the  $\ell = 0$  homoclinic bifurcations, exactly in the region where robust SAs exist. Thus only lower bounds and approximate curves for the regions where SAs are observed are found. We suspect that both phenomena (the failure of the SMF and the appearance of SAs) are associated with the involvement of the stable and unstable manifolds in a 1:1 resonance. Thus we derive a simple lower bound for  $\varepsilon$  above which the manifolds enter the 1:1 resonance [Eq. (25)]. The study of the relation between the resonance, the manifolds, and the SAs, and the construction of a more accurate approximation to the homoclinic bifurcation curves near a 1:1 resonance are left for future work.

The structure of the SAs varies with the parameters; as the ratio  $\delta/\gamma$  increases the values of the positive Lyapunov exponent slightly decrease and the Lyapunov (fractal) dimension decreases significantly. Surprisingly, we find that fixing this ratio and varying the other parameters in one of the “windows” for which SAs exist, the structure, Lyapunov exponent, and Lyapunov dimension of the SAs hardly change. Such a variation does change, in particular, the dissipation (area contracting) rate per Poincaré map.

**ACKNOWLEDGMENTS**

We thank Dimitri Turaev and A. A. Vasiliev for discussion and comments. This research is supported by MINERVA Foundation, Munich, Germany.

**APPENDIX: FINDING SECONDARY HOMOCLINIC BIFURCATION CURVES**

In this appendix some technical aspects regarding the method of solution of Eqs. (17)–(21) are described.

From Eqs. (17)–(21) we construct the equations

$$t_{1cd}^i(t_0) = M_d^{-1,i}(-M_c(t_0)) + j_{cd}T, \tag{A1}$$

$$\varepsilon_{cd}^i(t_0) = \begin{cases} \frac{P^{-1}(t_{1cd}^i(t_0) - t_0)}{M_c(t_0)}, & c = d \\ \frac{P^{-1}(2(t_{1cd}^i(t_0) - t_0))}{M_c(t_0)}, & c \neq d \end{cases} \tag{A2}$$

where  $c, d \in \{l, r\}$ ;  $i = 1, 2$ ;  $j_{cd} \in \mathbb{N}$ , and from Eq. (7) for the Melnikov function of the AFDO, one gets

$$M_d^{-1,1}(x) = \frac{1}{\omega} \arcsin\left(\frac{x}{\gamma F_d(\omega, \beta)} + \frac{4\delta}{3\gamma F_d(\omega, \beta)}\right),$$

$$M_d^{-1,2}(x) = \frac{\pi}{\omega} - \frac{1}{\omega} \arcsin\left(\frac{x}{\gamma F_d(\omega, \beta)} + \frac{4\delta}{3\gamma F_d(\omega, \beta)}\right).$$

Notice that  $M_d^{-1,i}(x)$  are undefined for

$$\left| \frac{x}{\gamma F_d(\omega, \beta)} + \frac{4\delta}{3\gamma F_d(\omega, \beta)} \right| > 1,$$

hence there are some values of  $t_0$  in  $[0, T)$  for which  $\varepsilon_{cd}^i(t_0)$  from Eq. (A2) are undefined. From Eqs. (20) and (23) we get that for  $t_0 \in [0, T)$ :  $j_{cd} = \ell_{cd} + s(t_0)$ , where  $s(t_0) = 0$  for  $t_0 \in [0, T/2)$ , and  $s(t_0) = 1$ , for  $t_0 \in [T/2, T)$ . The above equations [Eqs. (A1) and (A2)] are dependent on the perturbation parameters  $\beta$  (asymmetry),  $\delta$  (dissipation),  $\gamma$  (the amplitude of the forcing), and  $\omega$  (the frequency of the forcing). In addition, for  $|H| = |\varepsilon M_c(t_0)| \ll 1$  we get [see Eqs. (6), (21), (22), and (A1)]

$$0 = \frac{\partial h_2^{cd}(t_0, \varepsilon)}{\partial t_0} \approx M'_c(t_0) + M'_d(M_d^{-1,i}(-M_c(t_0))) \left(1 - \frac{M'_c(t_0)}{M_c(t_0)}\right), \quad (\text{A3})$$

$$c, d \in \{l, r\}, \quad i = 1, 2.$$

Hence for the AFDO Eq. (A1) becomes

$$t_{1cd}^1(t_0) = \frac{1}{\omega} \left[ 2\pi + \arcsin\left(-\frac{F_c(\omega, \beta)}{F_d(\omega, \beta)} \sin(\omega t_0) + \frac{8\delta}{3\gamma F_d(\omega, \beta)}\right) \right] + [\ell_{cd} + s(t_0)] \frac{2\pi}{\omega}, \quad (\text{A4})$$

$$t_{1cd}^2(t_0) = \frac{1}{\omega} \left[ \pi - \arcsin\left(-\frac{F_c(\omega, \beta)}{F_d(\omega, \beta)} \sin(\omega t_0) + \frac{8\delta}{3\gamma F_d(\omega, \beta)}\right) \right] + [\ell_{cd} + s(t_0)] \frac{2\pi}{\omega}, \quad (\text{A5})$$

$$s(t_0) = \begin{cases} 0, & t_0 \in \left[0, \frac{\pi}{\omega}\right) \\ 1, & t_0 \in \left[\frac{\pi}{\omega}, \frac{2\pi}{\omega}\right) \end{cases} \quad c, d \in \{l, r\}$$

and Eq. (A2) becomes

$$\varepsilon_{cd}^i(t_0) \approx \begin{cases} \frac{-16 \exp[t_0 - t_{1cd}^i(t_0)]}{\gamma F_c(\omega) \sin(\omega t_0) - 4\delta/3}, & c = d \\ \frac{16 \exp[t_0 - t_{1cd}^i(t_0)]}{\gamma F_c(\omega) \sin(\omega t_0) - 4\delta/3}, & c \neq d \end{cases} \quad (\text{A6})$$

$i = 1, 2.$

These approximations are valid for sufficiently small  $H$ 's of the period function [see Eq. (6)], namely, for

$$\varepsilon_{cc}^i(t_0) \left( \gamma F_c(\omega) \sin(\omega t_0) - \frac{4\delta}{3} \right) \rightarrow 0-, \quad (\text{A7})$$

$$\varepsilon_{cd}^i(t_0) \left( \gamma F_c(\omega) \sin(\omega t_0) - \frac{4\delta}{3} \right) \rightarrow 0+. \quad (\text{A8})$$

And, for such sufficiently small values of  $H$ , Eq. (A3) is

$$\frac{F_c(\omega, \beta)}{F_d(\omega, \beta)} \sin(\omega t_0) + \cos[\omega t_{1cd}^i(t_0)] \times \left( \tan(\omega t_0) - \frac{\omega \sin(\omega t_0)}{\sin(\omega t_0) - \frac{4\delta}{3\gamma F_c(\omega, \beta)}} \right) \approx 0, \quad (\text{A9})$$

where  $F_c, F_d$  are as in Eqs. (9) and (10) of Sec. II A for  $c, d \in \{l, r\}$ , and  $\varepsilon_{cd}^i(t_0)$  is calculated here with the use of the approximated value of the period function of AFDO,  $P(H)$ , from Eq. (6).

*Remark:* Since the exact inverse function of the period function of the AFDO,  $P^{-1}(x)$ , cannot be found analytically,  $(t_0^i, \varepsilon_{cd}^i(t_0^i))$ ,  $i = 1, 2$  are found by solving the equations

$$P(\varepsilon M_c(t_0)) = \tau_{cd}^i(t_0), \quad (\text{A10})$$

$$\frac{\partial P(\varepsilon M_c(t_0))}{\partial t_0} = \frac{\partial \tau_{cd}^i(t_0)}{\partial t_0}, \quad (\text{A11})$$

where

$$\tau_{cd}^i(t_0) = \begin{cases} t_{1cc}^i(t_0) - t_0, & M_c(t_0) < 0 \\ 2[t_{1cd}^i(t_0) - t_0], & M_c(t_0) > 0, \quad c \neq d \end{cases} \quad (\text{A12})$$

$$c, d \in \{l, r\}, \quad i \in \{1, 2\}, \quad t_0 \in [0, T), \quad T = \frac{2\pi}{\omega},$$

by a Newton method, combined with a linear prolongation scheme. As the initial guesses for the Newton method we use the approximated values for  $t_0^i$  and  $\varepsilon_{cd}^i(t_0^i)$ . See [27] for details on how these approximated values may be obtained.

When approximation to leading order in  $H$  for  $P(H)$  [as in Eq. (6)] is used to calculate  $\varepsilon_{cd}^i(t_0^i)$ , one gets that to leading order in  $\beta$ ,  $|\varepsilon_{cd}^i(t_0^i)| = |\varepsilon_{cc}^i(t_0^i)|$  for  $\delta = 0$ . Actually, more accurate approximations (such as using higher terms and Newton method) show that they are different.

- [1] J. Guckenheimer and P. Holmes, *Nonlinear Oscillations, Dynamical Systems, and Bifurcations of Vector Fields* (Springer-Verlag, New York, 1983).
- [2] F. C. Moon and P. J. Holmes, *J. Sound Vib.* **65**, 285 (1979).
- [3] F. C. Moon and P. J. Holmes, *J. Sound Vib.* **69**, 339 (1980).
- [4] S. Wiggins, *Introduction to Applied Nonlinear Dynamical Systems and Chaos* (Springer-Verlag, New York, 1990).
- [5] M. Golubitsky and I. Stewart (with appendix by J. Marsden), *Physica D* **24**, 391 (1987).
- [6] B. Ravindra and A. K. Mallik, *Phys. Rev. E* **49**, 50 (1994).
- [7] A. I. Neishtadt, *Fiz. Plazmy* **12**, 992 (1986) [*Sov. J. Plasma Phys.* **12**, 568 (1986)].
- [8] F. J. Bourland and R. Haberman, *SIAM J. Appl. Math.* **50**, 1716 (1990).
- [9] J. P. Eckmann and D. Ruelle, *Rev. Mod. Phys.* **57**, 617 (1985).
- [10] M. Benedicks and L. Carleson, *Ann. Math.* **133**, 73 (1991).
- [11] Y. L. Cao, *Sci. China Series A* **38**, 29 (1995).
- [12] M. Benedicks and L. S. Young, *Invent. Math.* **112**, 541 (1993).
- [13] L. Mora and M. Viana, *Acta Math.* **171**, 1 (1993).
- [14] V. Rom-Kedar, *Chaos* **5**, 385 (1995).
- [15] C. Soto-Treviño and T. J. Kaper, *J. Math. Phys.* **37**, 6220 (1996).
- [16] G. Haller and S. Wiggins, *Arch. Ration. Mech. Anal.* **130**, 25 (1995).
- [17] T. J. Kaper and G. Kovačič, *Trans. Am. Math. Soc.* **348**, 3835 (1996).
- [18] R. Camassa, G. Kovačič, and S. K. Tin (unpublished).
- [19] J. Palis and F. Takens, *Hyperbolicity & Sensitive Chaotic Dynamics at Homoclinic Bifurcations*, Cambridge Studies in Advanced Mathematics Vol. 35 (Cambridge University Press, Cambridge, England, 1993).
- [20] N. K. Gavrilov and L. P. Šilnikov, *Math. USSR Sb.* **88**, 467 (1972).
- [21] N. K. Gavrilov and L. P. Šilnikov, *Math. USSR Sb.* **90**, 139 (1972).
- [22] S. V. Gonchenko, L. P. Šilnikov, and D. V. Turaev, *Physica D* **62**, 1 (1993).
- [23] Y.-C. Lai, C. Grebogi, J. A. Yorke, and I. Kan, *Nonlinearity* **6**, 779 (1993).
- [24] E. Ott, *Chaos in Dynamical Systems* (Cambridge University Press, Cambridge, England, 1993).
- [25] V. Rom-Kedar, in *Transport, Chaos and Plasma Physics*, edited by F. Doveil, S. Benkadda, and Y. Elskens (World Scientific, Singapore, 1994).
- [26] V. Rom-Kedar, *Nonlinearity* **7**, 441 (1994).
- [27] A. Litvak-Hinenzon, M.Sc. thesis, Weizmann Institute of Science, Rehovot, Israel, 1996.
- [28] F. A. McRobie, *Philos. Trans. R. Soc. London Ser. A* **338**, 557 (1992).
- [29] R. W. Easton, *Trans. Am. Math. Soc.* **294**, 714 (1986).
- [30] B. V. Chirikov, *Phys. Rep.* **52**, 263 (1979).
- [31] D. F. Escande, in *Plasma Theory and Nonlinear and Turbulent Processes in Physics*, Proceedings of the International Workshop, Kiev, 1987, edited by V. G. Bar'yakhtar *et al.* (World Scientific, Singapore, 1988).
- [32] V. Rom-Kedar, *Physica D* **43**, 229 (1990).
- [33] G. M. Zaslavskii and N. N. Filonenko, *Zh. Eksp. Teor. Fiz.* **54**, 1590 (1968) [*Sov. Phys. JETP* **25**, 851 (1968)].
- [34] DSTOOLS, computer program, Cornell University, Center of Applied Mathematics, Ithaca, NY 14853.
- [35] A. Wolf, J. B. Swift, H. L. Swinney, and J. A. Vastano, *Physica D* **16**, 285 (1985).
- [36] A. H. Nayfeh and B. Balachandran, *Applied Nonlinear Dynamics*, Wiley Series in Nonlinear Science (Wiley, New York, 1995).
- [37] S. Pelikan and Z. Wan, *J. Dyn. Differ. Equ.* **4**, 667 (1992).
- [38] L. S. Young, *Physica A* **124**, 639 (1984).
- [39] Y. Ueda, S. Yoshida, H. B. Stewart, and J. M. T. Thompson, *Philos. Trans. R. Soc. London, Ser. A* **332**, 169 (1990).
- [40] J. M. T. Thompson, H. B. Stewart, and Y. Ueda, *Phys. Rev. E* **49**, 1019 (1994).
- [41] C. Grebogi, E. Ott, and J. A. Yorke, *Physica D* **24**, 243 (1987).